

EVALUATING ANTARCTIC SEA ICE VARIABILITY AND ITS TELECONNECTIONS IN GLOBAL CLIMATE MODELS

JIPING LIU^{a,b,*}, DOUGLAS G. MARTINSON^{b,c}, XIAOJUN YUAN^c and DAVID RIND^{a,b}

^a NASA/Goddard Space Flight Center, Institute for Space Studies, New York, NY 10025, USA

^b Department of Earth and Environmental Sciences, Columbia University, Palisades, NY 10964, USA

^c Lamont–Doherty Earth Observatory of Columbia University, Palisades, NY 10964, USA

Received 20 February 2001

Revised 3 January 2002

Accepted 6 January 2002

ABSTRACT

This study evaluates simulated Antarctic sea ice edge (SIE) variability and its teleconnections in three global coupled climate models (GISS, NCAR and GFDL) against the observations. All models do a reasonable job in simulating the seasonal advance and retreat of the Antarctic sea ice fields. The simulated GISS and NCAR SIE distributions are in agreement with observations in summer and autumn, whereas the GFDL model does best in spring and winter. A common problem is the poor simulation of the observed SIE in the Weddell Sea. All models are not particularly good at simulating the observed regionally varying SIE trends. A comparison of dominant empirical orthogonal function modes of surface air temperature (SAT) variability in each model associated with observed modes show that the models generally capture features of the more prominent covarying spatial patterns such as an El Niño–southern oscillation (ENSO)-like pattern in the tropical Pacific.

The simulated teleconnection patterns between detrended Antarctic SIE anomalies and detrended global SAT anomalies in each model are evaluated for comparison with observed teleconnection patterns. All models capture the ENSO-like phenomenon to some degree. Also, the GISS and NCAR models capture the Antarctic dipole pattern and meridional banding structure through the Pacific. The Antarctic SIE regions showing the strongest extrapolar teleconnections differ among the models and between the models and observations. Almost all models miss the observed polar–extrapolar teleconnections in the central Indian, western extreme of the tropical and southern Pacific, and over the tropical continents. Copyright © 2002 Royal Meteorological Society.

KEY WORDS: Antarctic sea ice edge; global climate models; teleconnection patterns; ENSO; Bellingshausen, Amundsen, Ross and Weddell Seas

1. INTRODUCTION

Sea ice plays an important role in the state and variability of regional and global climate through thermodynamic and dynamic processes, and feedback mechanisms operating over a hierarchy of space and time scales (e.g. Walsh, 1983). This role is largely attributed to the ice–albedo feedback, the insulating effect of sea ice, and its influence on the global thermohaline circulation through salt rejection during ice growth and surface freshening during ice melt.

One of the noticeable impacts of sea ice is the poleward amplification of global warming in observed surface air temperature (SAT) in both hemispheres (Gates *et al.*, 1996; Flato and Boer, 2001). However, climate-change simulations in global coupled climate models typically show a marked hemispheric asymmetry, with more warming in the northern high latitudes than in the south (Kattenberg *et al.*, 1996). This asymmetry might be ascribed to simplified treatments of sea ice and ocean processes (Flato and Boer, 2001). Experiments with sea ice models (Hibler, 1984; Lemke *et al.*, 2000) have shown that models including only sea ice

*Correspondence to: Jiping Liu, 2880 Broadway, NASA/Goddard Space Flight Center, Institute for Space Studies, New York, NY 10025, USA; e-mail: jliu@giss.nasa.gov

thermodynamics are more sensitive to changes in the thermal forcing than those that include dynamics. The inclusion of sea ice dynamics is particularly important in the Southern Ocean (Pollard and Thompson, 1994). One study (Rind *et al.*, 1995) showed that feedback associated with sea ice variability accounts for over one-third of the $2 \times \text{CO}_2$ global warming in the Goddard Institute for Space Studies (GISS) general circulation model (GCM; Hansen *et al.*, 1983), which further indicates the importance of incorporating realistic sea ice physics in climate models. The IPCC assessment (Gates *et al.*, 1996) showed that the largest disagreement among global climate model simulations of present climate is in the polar regions. This disagreement among the models reflects our limited understanding of the sensitivity of climate models to sea ice variability, dramatically different sea ice treatments and each model's ability to represent the complex interactions, leading to polar–global covariability. Rind *et al.* (1997) suggest that sea ice variability has a strong influence on the climate model sensitivity; specifically, the sensitivity depends on sea ice *extent* in the Southern Hemisphere. All aforementioned studies suggest that sea ice variability and associated feedback mechanisms play a significant role in determining climate sensitivity and simulations.

We believe that an important diagnostic of the climate models' ability to simulate sea ice variability and its climate-relevant influences can be assessed by evaluating the extent to which the model can capture observed polar–global covarying climate structure. Evidence of the El Niño–southern oscillation (ENSO) teleconnections in southern high latitudes has been identified in many studies (Smith and Stearns, 1993; Gloersen, 1995; Simmonds and Jacka, 1995). In a recent study, Yuan and Martinson (2000) evaluated Antarctic sea ice variability and quantified its global climate teleconnections. They investigated systematic lagged linear correlations between Antarctic detrended sea ice edge anomalies (SIE*) and global climate variables, including large-scale indices and detrended anomalies in surface air temperature (SAT*). Their results showed considerably more high-correlation teleconnections between Antarctic SIE* and global climate than expected from correlating coloured, quasi-periodic noise. Those teleconnection patterns most likely to represent physically meaningful teleconnection patterns are identified; their presence and global distribution imply significant meridional communications between the polar and extrapolar (mid-latitudes, subtropics and tropics) regions. These patterns thus represent diagnostics against which to evaluate the climate models to see if changes in model SIE*, comparable to that observed in nature, are associated with globally covarying patterns also observed in nature.

The purpose of this paper is to assess whether or not current US global coupled climate models have the capability to capture these teleconnection patterns. To achieve this goal, we repeat the Yuan and Martinson (2000) statistical analysis by analysing the output from three state-of-the-art global coupled climate models: the GISS, National Center for Atmospheric Research (NCAR) and NOAA's Geophysical Fluid Dynamics Laboratory (GFDL) models. We use the results of these analyses to determine the extent to which the models capture observed polar–extrapolar teleconnections, and to design follow-up experiments in an attempt to deduce the underlying mechanisms responsible for producing the teleconnections. In this paper, we focus on the comparison between the simulated Antarctic sea ice characteristics and their global teleconnections relative to those present in the observations.

2. DESCRIPTIONS OF GLOBAL CLIMATE MODELS

Here, we briefly review the relevant features in each model, concentrating on those features that affect sea ice simulations. More complete descriptions of each model can be found in the references provided. Higher resolution and improved versions of the models from each of the groups have recently been developed, which may indeed do a better job in simulating air–sea-ice interactions. However, these models have not yet undergone widespread testing and the results of the CO_2 scenario runs are not generally available, though we are working with members from each of the groups to perform a similar analysis with those model results in a future paper. Currently, evaluations of the standard versions are presented here. Descriptions of the horizontal and vertical resolution for each model are listed in Table I for comparison.

Table I. Model horizontal and vertical resolution (lat: latitude; lon: longitude)

Coupled model	Atmosphere component	Ocean component	Sea ice component
GISS	4° lat × 5° lon, 9 layers	4° lat × 5° lon, 13 layers	4° lat × 5° lon, 4 layers
NCAR	2.8° lat × 2.8° lon, 18 layers	2.4° lon, 1.2° lat in the tropics (< 20 °) and high latitudes (> 60 °) and 2.3° lat in mid-latitudes; 45 layers	2.4° lon, 1.2° lat in the tropics (< 20 °) and high latitudes (> 60 °) and 2.3° lat in mid-latitudes; 3 layers
GFDL	4.5° lat × 7.5° lon, 9 layers	4.5° lat × 3.75° lon, 12 layers	4.5° lat × 3.75° lon, 1 layer

2.1. GISS coupled climate model

The atmospheric component of the GISS coupled climate model (Russell *et al.*, 1995, 2000) is similar to that of Hansen *et al.* (1983) except that atmospheric conservation equations for mass and momentum are solved on an Arakawa C grid, and advection of potential enthalpy and water vapour uses a linear upstream scheme (Russell and Lerner, 1981). The ocean component conserves mass, has a free surface, applies the linear upstream scheme for the advection of potential enthalpy and salt, and employs the KPP vertical mixing scheme of Large *et al.* (1994). Atmospheric and oceanic surface fluxes are solved and applied synchronously. Flux adjustments are not used.

The sea ice thermodynamics conserve mass and energy (Russell *et al.*, 1995). Sea ice cover is determined by energy exchange with the atmosphere, and by the ocean heat transport and heat capacity. When surface fluxes calculated from the model tend to cause the open ocean fraction to cool below the freezing point, the ocean stays at the freezing point and sea ice is formed with minimum thickness (0.2 m) and areal concentration required to conserve thermal energy while realizing the minimum thickness. If the sea-ice-covered fraction extracts sufficient heat from the ocean to cool it below freezing point, then the ocean stays at the freezing point and sea ice thickens. If the open ocean fraction becomes less than the minimum lead criteria (6%), then sea ice is contracted horizontally to increase its thickness to maintain this minimum lead area constraint. Since sea ice contains no salt, the salinity of the uppermost ocean layer increases as sea ice grows thermodynamically. The spectrally integrated sea ice albedo varies from 0.45 for sea ice without snow to 0.95 for sea ice with deep snow. The sea ice dynamics follow the cavitating fluid rheology of Flato and Hibler (1992), with a few modifications.

2.2. NCAR climate system model

Each model component of the NCAR coupled model is linked by a flux coupler (no flux correction), which simultaneously computes the interfacial fluxes between components (Bryan, 1996). The atmosphere and ocean dynamics involve a spectral transform method in which T42 signifies spectral triangular truncation at wave-number 42 for dynamical variables. The NCAR atmospheric component represents a wide range of parameterized physical processes, such as the effects of clouds, water vapour, greenhouse gases and ozone on the radiation (Kiehl *et al.*, 1998). The ocean includes the eddy-mixing (Gent and McWilliams, 1990) and KPP vertical-mixing parameterizations (Large *et al.*, 1994), as well as a third-order upstream differencing scheme for heat and salt (NCAR OS, 1996; Gent *et al.*, 1998).

The sea ice thermodynamics are based on the Semtner (1976) model, with minor modification for its interface with the flux coupler. The flux exchanges of heat, water and momentum are computed separately within the ice-covered and ice-free fractions of each grid box to include the effect of leads on climate. Cooling the ocean temperature beyond the freezing point (primarily in leads) produces lateral ice growth (increasing sea ice concentration), whereas heat loss via conduction through existing sea ice increases its thickness. Maximum sea ice concentrations (99% in the Northern Hemisphere, 96% in the Southern Hemisphere) are imposed to allow for the existence of leads in thick pack ice. The computation of sea ice albedo (ranging

from 0.5 to 0.82) depends on snow cover/depth and surface temperature. The sea ice extent in the NCAR model is constrained not to exceed 60°S (though observations show ice as far north as 55°S during winter). The sea ice dynamics employ the cavitating fluid rheology of Flato and Hibler (1992). Ice velocity is solved on an Arakawa B grid, following a modified Pollard and Thompson (1994) advection scheme.

2.3. GFDL coupled climate model

The GFDL coupled climate model consists of a R15 (rhomboidal truncation) atmospheric component (Gordon and Stern, 1982), which is coupled to an ocean component described by Bryan and Lewis (1979). Atmospheric dynamics involve the spectral transform method, and the resolution is limited by a cutoff beyond wave-number 15. The effects of clouds, water vapour, CO₂ and ozone are included. For the ocean component, sub-grid scale motion is approximated via turbulent viscosity or turbulent diffusion. To reduce model climate drift, flux corrections of heat and water are imposed at the ocean surface (including sea-ice-covered areas).

Sea ice forms when the ocean surface layer would otherwise cool below the freezing point. The sea ice thickness is directly augmented by snowfall and by local freezing proportional to the difference between the heat lost to the atmosphere and that supplied by the underlying ocean. The sea ice temperature is predicted from a net balance of the surface energy fluxes and a conduction flux from the underlying ocean (heat exchange through leads is neglected). Following Broccoli and Manabe (1987), sea ice albedo depends on surface temperature and sea ice thickness, and ranges from 0.55 to 0.8. The sea ice dynamics are similar to the simple free drift model developed by Bryan (1969) that incorporates the horizontal advection of sea ice by ocean currents, but does not include wind-induced ice drift. The sea ice moves freely with the surface ocean currents provided that its thickness is less than 4 m, but it is stationary for higher thickness.

3. DATA

3.1. Observed data

Yuan and Martinson (2000) investigated Antarctic SIE variability and its global teleconnections using: (1) National Centers for Environmental Prediction (NCEP) and NCAR reanalysis SAT at 1000 hPa (Kalnay *et al.*, 1996); (2) 19 years of sea ice concentration observed by satellite SMMR/SSM/I (Nimbus-7 Scanning Multichannel Microwave Radiometer and Spatial Sensor Microwave Imagers) sensors. See Yuan and Martinson (2000) for more detailed discussions regarding these data and their reliability.

3.2. Model output

In this study, for comparison with Yuan and Martinson (2000), we interpolated the monthly SAT of the scenario run (described below) results of the GISS, NCAR and GFDL models onto a 5° × 5° grid from January 1977 through to December 1999 (except for the NCAR results, which are from 1977 to 1997). Monthly SAT anomalies were generated by removing the monthly SAT climatology within each grid cell (based on the data for the same time period). We then eliminated any trend present in the anomalies at each grid cell to generate SAT*.

The scenario runs are transient experiments involving increasing atmospheric concentrations of CO₂. For the GISS scenario run, observed greenhouse gases are used from 1950 to 1990; then the CO₂ increases 1% per year from 1991 to 2099. Tropospheric sulphate aerosols, varying annually according to the UK Meteorological Office (UKMO; Mitchell *et al.*, 1995), are included in the radiation balance. The NCAR scenario simulation runs from 1870 through to 1998; it is initialized with 1870 conditions. The observed sulphate and greenhouse gas forcings are ramped through the simulation. For the GFDL scenario run, initial CO₂ concentration is approximately equal to the 1958 concentration, after which CO₂ increases 1% per year, which is approximately equal to the rate of total radiative forcing of all the greenhouse gases of the IPCC (Gates *et al.*, 1996) 'business-as-usual' scenario. The average global SAT has risen 0.72°C, 0.55°C and 0.84°C during the above study period in the GISS, NCAR and GFDL models respectively. Antarctic

sea ice concentration results for the GISS and NCAR models were interpolated onto a 0.25° (latitude) and 1° (longitude) grid. Consistent with Yuan and Martinson (2000), monthly SIE is defined as the equatorwardmost position of the 30% isopleth of sea ice concentration for each degree of longitude. If the 30% sea ice concentration is not found in any latitude, the SIE is given as the Antarctic coastline latitude. The SIE is averaged into 12° longitude bands to generate 30 quasi-spatially independent time series separated in space by the average spatial decorrelation length in the observations (Yuan and Martinson, 2000). As with SAT*, SIE anomalies about the monthly climatological values for each 12° longitude band were computed and detrended to generate SIE*. Because the sea ice concentration is not an output diagnostic variable of the GFDL model, we use 20 cm sea ice thickness in that model to define the SIE position. This is approximately equivalent to the 30% sea ice concentration (Stouffer, personal communication). Note that all data were filtered to remove sub-annual variability before generating detrended anomalies.

4. RESULTS

4.1. Climate model performance

Before evaluating whether or not the observed teleconnections between Antarctic SIE* and global SAT* in Yuan and Martinson (2000) are captured in the model simulations, it is helpful to assess if the observed SIE characteristics (the SIE distributions and trends reflect a strong interaction between atmosphere, ocean and sea ice dynamics and thermodynamics, including the general distribution of the Antarctic Circumpolar Current, which serves as the boundary between the polar and subtropical ocean basins) and dominant covarying spatial patterns in SAT* are well simulated. Based upon this analysis, we can obtain a preliminary understanding of the performance of these models.

4.1.1. Antarctic SIE characteristics. The observed and simulated seasonal mean SIE is shown in Figure 1. Overall, all models do a reasonable job in simulating the seasonal advance and retreat of the Antarctic sea ice fields. The simulated GISS and NCAR SIE distributions are similar to the observed SIE in summer and autumn, and the simulated GFDL SIE is closest to the observed SIE in spring and winter. In general, the GISS model produces excess sea ice cover, except between the eastern Indian and the western extreme of the western Pacific sectors of the Antarctic. GISS SIE extends $4\text{--}5^\circ$ of latitude farther north than observed winter SIE in the eastern Pacific sector of the Antarctic and the Weddell Sea. The difference can be as large as 8° latitude in the same region in spring. By contrast, NCAR produces less sea ice cover than the observations, especially in the Western Hemisphere. The NCAR SIE is $4\text{--}5^\circ$ farther south than observed SIE in the eastern Ross Sea, the eastern Pacific sectors of the Antarctic and the Weddell Sea in spring, but is in close agreement with observed SIE in most regions in winter (due to the limitations imposed by its 60°S cut-off). The GFDL model generates excess sea ice cover between the eastern Indian and western Pacific sectors of the Antarctic and in the Weddell Sea in summer and autumn.

Because of our ready access to extensive GISS model diagnostics, we analyse the GISS results to determine why this model produces an excess sea ice cover in the aforementioned regions. Figure 2 shows the observed (Levitus and Boyer, 1994; Levitus *et al.*, 1994) and simulated vertical ocean temperature and salinity profile along 107.5°E , 107.5°W and 32.5°W in September (winter maximum sea ice extent). Compared with Levitus and co-workers (Levitus and Boyer, 1994; Levitus *et al.*, 1994), the simulated temperature is colder and more homogeneous in the upper ocean layer of the Weddell Sea (32.5°W). This greatly reduces the contribution of heat from the relatively warm deep water into the surface layer, this being necessary to maintain the thin winter sea ice cover (Martinson, 1990). The simulated upper ocean layer is also fresher than that of Levitus and co-workers (Levitus and Boyer, 1994; Levitus *et al.*, 1994), which works to reduce the upward mixing of the warm underlying deep water in the mixed layer as well, further limiting the ability of the ocean to maintain a thin ice cover. The situation is similar in the eastern Pacific sector of the Antarctic (107.5°W). By contrast, the simulated temperature of the upper ocean layer is warmer compared with Levitus and co-workers (Levitus and Boyer, 1994; Levitus *et al.*, 1994) along 107.5°E , so less sea ice forms between the eastern Indian and the western extreme of the western Pacific sectors of the Antarctic.

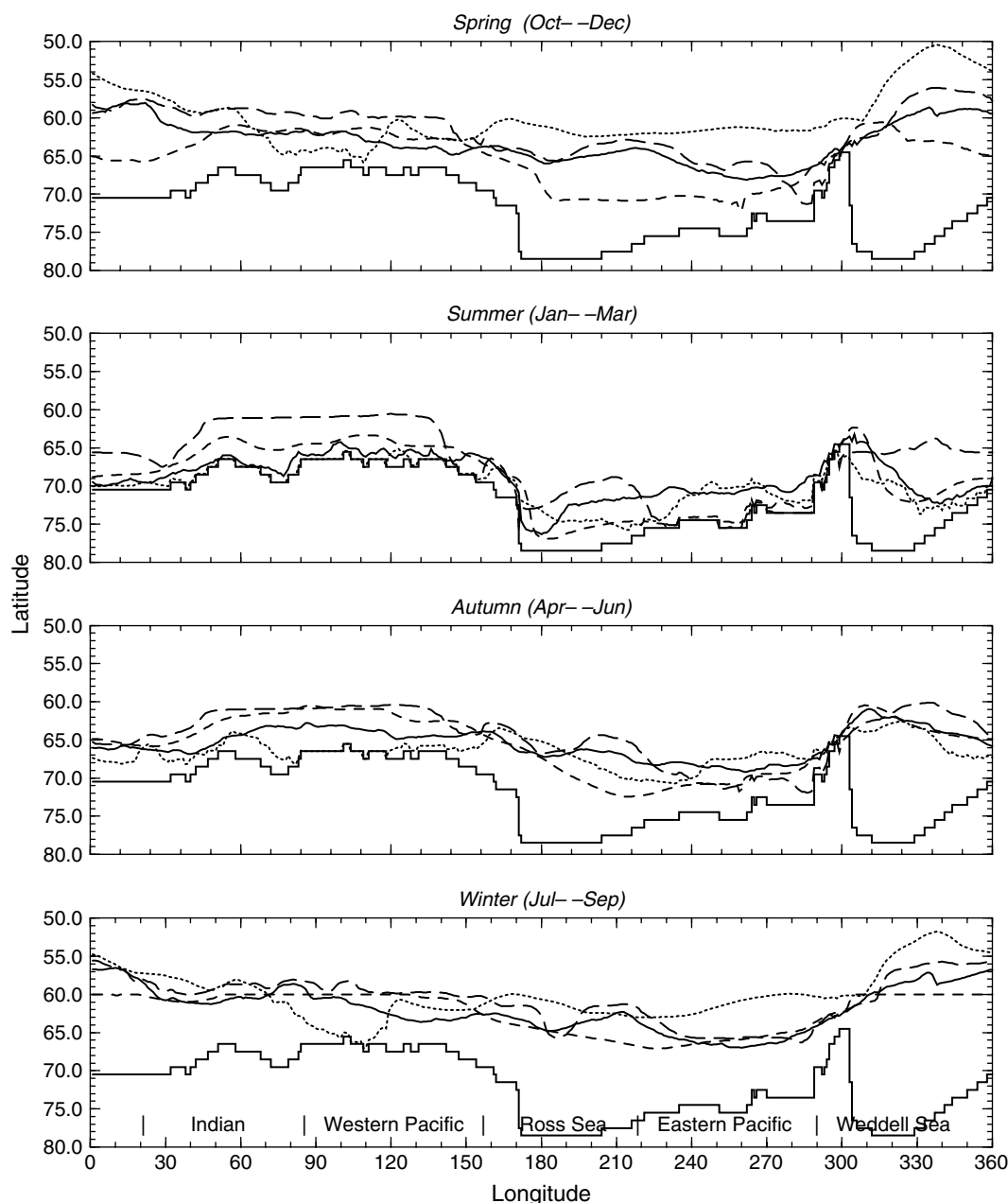


Figure 1. The seasonal Antarctic SIE (in degree latitude); solid line: SMMR/SSM/I satellite observation; dotted line: GISS; dashed line: NCAR; short-long dashed line: GFDL; stair line: Antarctic continent

A linear regression is applied to the observed and simulated SIE anomalies as a function of longitude to estimate SIE trends (Figure 3; Weatherhead *et al.*, 1998). Overall, the models are not good at simulating the observed, regionally varying SIE trends (retreating in the Bellingshausen and Amundsen Seas and expanding in the Ross and Weddell Seas) found by Yuan and Martinson (2000). The GISS and NCAR models produce an overall decreasing trend of 4.9% and 2.4% degree/year respectively. The GFDL results have no significant net SIE trend, which is consistent with the circumpolar-wide average observational results. (Gloersen and Campbell, 1991; Cavalieri *et al.*, 1997; Yuan and Martinson, 2000). The general inability to capture the

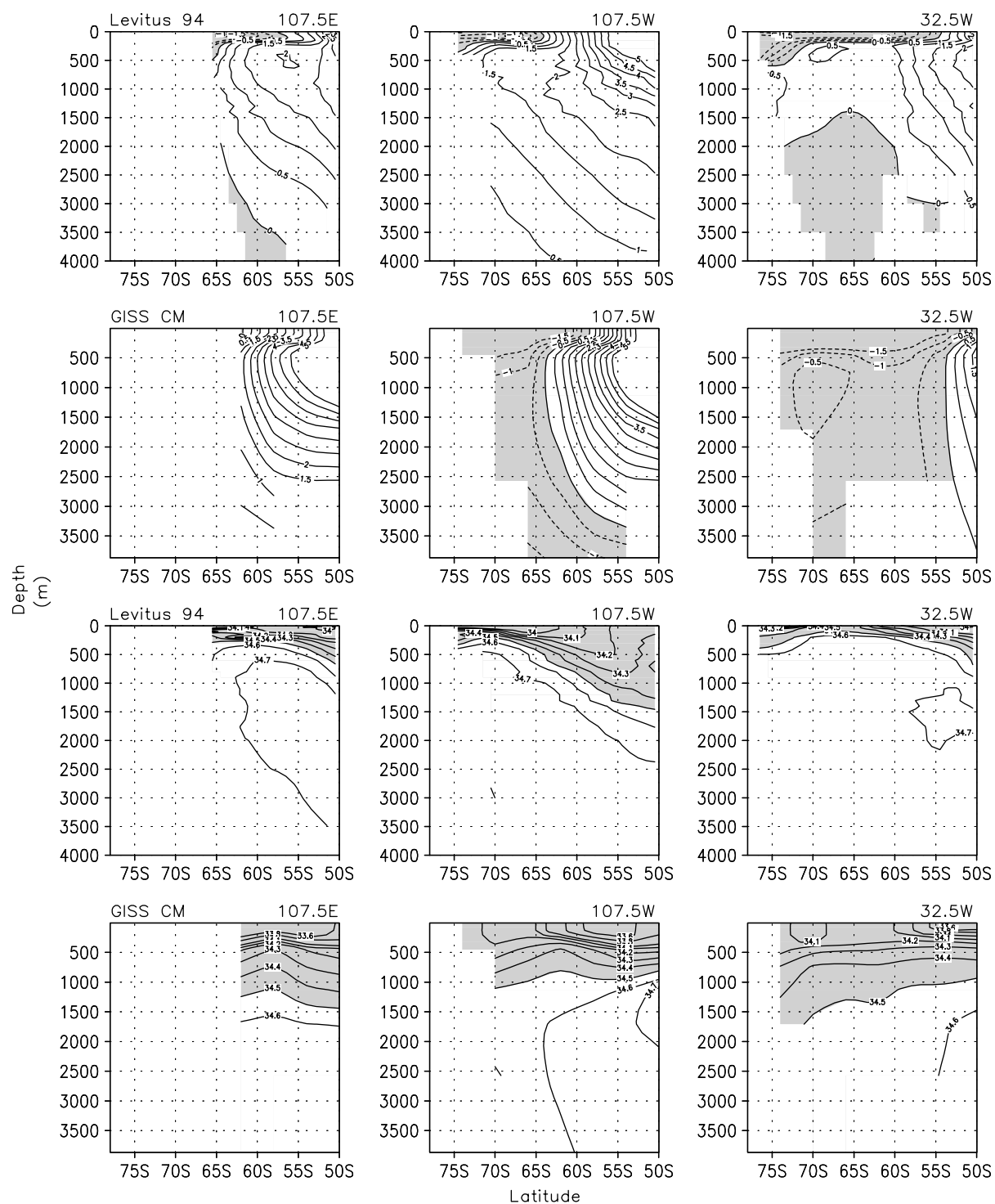


Figure 2. The vertical ocean temperature (upper two rows) and salinity (lower two rows) profiles along 107.5°E, 107.5°W, 32.5°W in September from Levitus and co-workers (Levitus and Boyer, 1994; Levitus *et al.*, 1994) and the GISS model (the temperature below 0°C, salinity below 34.5 ppt are shaded)

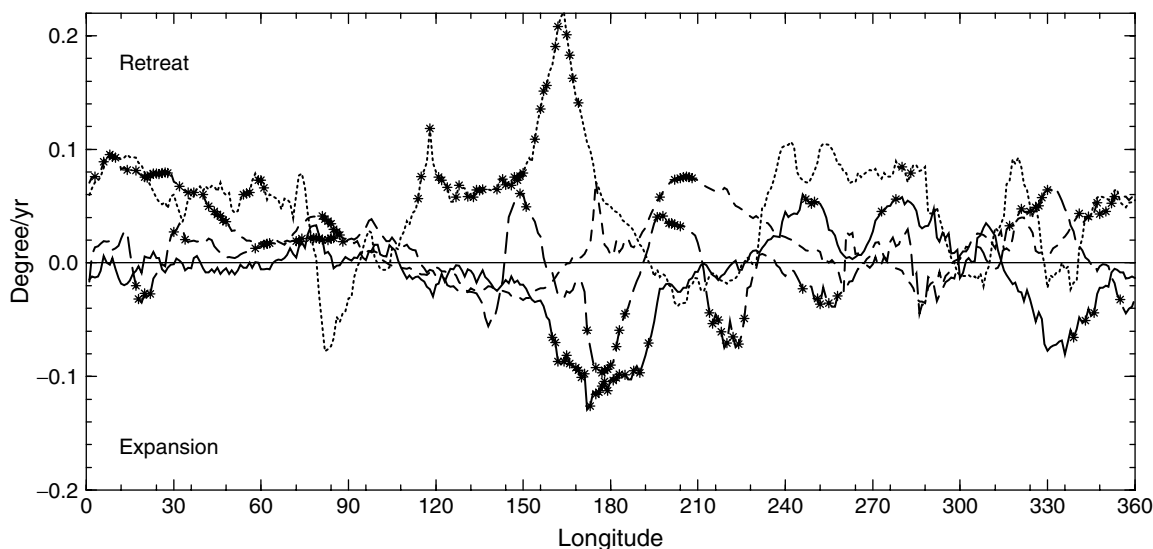


Figure 3. The linear Antarctic SIE anomaly trends (in degrees latitude); solid line: SMMR/SSM/I satellite observation; dotted line: GISS; dashed line: NCAR; short-long dashed line: GFDL. Asterisks: SIE trends above 95% confidence level

trends may reflect inconsistencies between reality and model-imposed forcings, and weak parameterizations of any of the regional or local physics influencing SIE simulations.

4.1.2. SAT characteristics. In an attempt to determine if dominant covarying spatial climate patterns in each model (as indicated by SAT* distributions) are consistent with spatial distributions of known climate patterns identified in Yuan and Martinson (2000), an empirical orthogonal function (EOF) analysis for SAT* (using correlation matrices) of each model is performed. EOFs are sensitive to many parameters, so we do not expect identical matches, but rather use this approach to see if the primary characteristics of the dominant patterns are simulated.

As a basis for subsequent comparisons, the three leading observation-based EOFs described in Yuan and Martinson (2000) (Figure 4(a)) are presented here from a global perspective (the notation adopted here consists of a letter E denoting EOF, followed by the mode number and data source in parentheses): (1) E1(NCEP) contains a considerable segment of the tropical Atlantic and Indian, as well as the tropical continents, particularly South America and Africa; (2) E2(NCEP) represents the tropical Pacific ENSO-like pattern, including the central Indian component; (3) E3(NCEP) has a strong negative correlation between (a) the western extreme of the tropical and southern Pacific and (b) the eastern tropical Pacific and eastern Pacific sector of the Antarctic. These modes represent 14%, 11% and 10% of the total SAT* variance respectively. From a circumpolar perspective, an out-of-phase relationship exists between the eastern Pacific sector of the Antarctic and the Weddell Sea; Yuan and Martinson (2000) refer to this as the Antarctic dipole.

Figure 4(b)–(d) shows the first three modes extracted from the model-based SAT* for the GISS, NCAR and GFDL results respectively. All the models simulate the tropical Pacific ENSO-like pattern of E2(NCEP) to some degree. E1(GFDL) (Figure 4(d1), which accounts for 11% of the total variance) seems to simulate the observed maximum SAT* variability well in the central and eastern Pacific due to the ENSO phenomenon, but the central Indian component is too narrow and weak. The GISS model does not produce a different phase relationship between the tropical eastern and western Pacific (Figure 4(b2)), whereas the NCAR results barely capture the observed covarying maximum SAT* variation in the central Indian (Figure 4(c3)). Qualitatively, the main spatial characteristics of E3(NCEP) are partially captured by the NCAR (Figure 4(c2)) and GFDL results (Figure 4(d3)), though the simulated SAT* variability is too small in the western tropical Pacific. None of the three models captures the main features in E1(NCEP), especially the strong in-phase relationship between tropical South America and Africa. Note that the simulated SAT* variability in the tropics, especially



Figure 4. The first three leading EOF mode eigenvectors of the NCEP–NCAR reanalysis of SAT* (a) and simulated SAT* in the GISS (b), NCAR (c) and GFDL (d) models

over the continents, is underestimated in all the models. Generally speaking, the models capture the observed patterns somewhat, but the coarse resolution of these models is not good enough to simulate the atmospheric responses to ENSO events and leads to reduced amplitude of simulated ENSO events.

4.2. Polar–extrapolar teleconnections

The statistically significant (accounting for autocorrelation in space and time) teleconnection patterns identified in Yuan and Martinson (2000) are presented here to facilitate comparison with the model-produced teleconnections. The teleconnections are identified by correlating the 30 Antarctic SIE* time series with SAT* time series in each global grid cell at half year lag intervals up to ± 2 years. This generates a total of 270 global correlation maps that were analyzed by Yuan and Martinson (2000). The global correlation maps involving SIE* between the eastern Weddell Sea and the western Indian sector of the Antarctic (*section A*) and between the Bellingshausen and western Weddell Seas (*section B*) at zero lag display a clear ENSO-like pattern (Figure 5(a1,a2)) as well as a tropical Atlantic variability (TAV) pattern (Kushnir *et al.*, 1997). Note that despite the similarity between the correlation map patterns and the major established climate patterns (e.g. ENSO and TAV), Yuan and Martinson (2000) performed a significance test that showed there were considerably more significant polar–extrapolar correlations than would be expected due to the spatial coherence inherent in these global climate patterns to begin with. These findings suggest that the SIE* in the aforementioned regions has potentially strong links with ENSO and TAV. These same general patterns reappear in correlation maps for other time lags and for different SIE* regions in the circumpolar belt, displaying an eastward propagation in SIE* lagged correlations consistent with an eastward propagating SIE* signal associated with the Antarctic circumpolar wave (White and Peterson, 1996). Figure 5(a3) presents the correlation features involving SIE* in the eastern Pacific sector of the Antarctic and Weddell Sea at zero lag. There is a significant negative correlation between the eastern Pacific sector of the Antarctic and western extreme of the tropical and southern Pacific, as well as a meridional banding structure in the Pacific and Atlantic. In addition, the Antarctic dipole repeatedly appears, with the strongest relationship at zero lag (Figure 5(a3)). In order to investigate how well each model captured the observed spatial and temporal distribution of polar–extrapolar climate links found in Yuan and Martinson (2000), we repeated the same lagged correlations between simulated Antarctic SIE* and simulated global SAT* for each model.

The correlation maps based on the GISS model output capture: (1) the Antarctic dipole (Figure 5(b3)); (2) the meridional banding structure present through the Pacific (Figure 5(b3)); and (3) the general ENSO-like pattern, though the pattern is much more extensive across the entire tropics (at zero lag) than found in the observations (Figure 5(a1,a2)). The SIE* regions in the model linked to the ENSO-like pattern involve the western Indian sector of the Antarctic (Figure 5(b1)) and the Bellingshausen Sea (Figure 5(b2)). The former is east of *section A* (Figure 5(a1)) in the observations, whereas the latter is slightly narrow relative to *section B* (Figure 5(b2)) in the observations. Also, the degree of model-generated polar–extrapolar correlation of the ENSO-like correlation pattern is smaller than found in the observations (given that the correlations in the eastern tropical Pacific show more shared variance r^2 in the observations relative to the model). Compared with the observations, this ENSO-like pattern irregularly appears in correlation maps involving other time lags. Therefore, the GISS model apparently simulates the linkage between the Antarctic SIE* and the ENSO-like pattern to some extent. This is an unexpected success, given the following GISS model results: (1) the GISS model overestimates sea ice cover in the eastern Pacific sector of the Antarctic and Weddell Sea in winter and spring, where sea ice was found to be sensitive to the ENSO variation in the observations; (2) the amplitude of the ENSO index simulated in the GISS model is weaker than the observed ENSO index.

The NCAR model reproduces the weak connectivity between the Antarctic SIE* and the ENSO-like pattern in the tropics. Correlation between simulated SIE* in the central Indian sector of the Antarctic and western Weddell Sea and SAT* does generate a much narrower and weaker ENSO-like pattern (Figure 5(c1,c2)). This narrow and weak ENSO-like pattern appears sporadically at other time lags. Therefore, the NCAR model generates the weak linkage between SIE* and ENSO events. The reason for this failure may reflect the limit of



Figure 5. The linear correlation between the NCEP-NCAR reanalysis SAT* and satellite SIE* (a), between the simulated SAT* and SIE* of the GISS (b), NCAR (c) and GFDL (d) in the underlined regions at zero lag. Cross-correlations significant at the 95% confidence level are 0.44, 0.41 and 0.26 in the GISS, NCAR and GFDL models respectively (taking into account at temporal autocorrelations presented in the dataset; see Yuan and Martinson (2000) for detailed discussion)

sea ice extent in the NCAR model (recall that the sea ice is not allowed to expand equatorward of 60°S). This greatly constrains the variability of SIE^* in the Weddell Sea, which is a sensitive region to the ENSO signal. Additionally, the NCAR model produces roughly 55%–60% of the amplitude of the observed ENSO (Meehl and Arblaster, 1998). The Antarctic dipole is simulated well by the NCAR model, though the Weddell pole is displaced westward (Figure 5(c3)). The meridional banding structure also shows up in the NCAR results, but the SIE^* regions linked to this structure are spatially incorrect.

As with the GISS and NCAR models, the GFDL model also captures the ENSO-like correlation pattern to some extent. The SIE^* regions most strongly linked to the ENSO-like pattern are the central western Pacific sector of the Antarctic and the central Ross Sea at zero lag, which differs from *sections A* and *B* in the observations (Figure 5(d1,d2)). The ENSO-like pattern is much weaker, but it regularly appears at the same location for other time lags. The Antarctic dipole and meridional banding structure are not obvious in the GFDL model results at zero lag. Simple sea ice dynamics (only ocean advection) in the GFDL model might be responsible for the above failures, since wind advection is necessary to give more realistic sea ice simulations. Like its counterparts, the GFDL model also produces low ENSO amplitude (<http://www.gfdl.gov/~gth/AR97>).

For each observed and simulated correlation map, significance tests are conducted to determine how many significant correlations are obtained beyond that expected given the coherent spatial/temporal covariability inherent in the SAT^* fields (see Yuan and Martinson (2000) for a detailed discussion). Distributions of fractions of grid points in each correlation map that pass the local 95% significance test as functions of SIE band and leading and lagging intervals are shown in Figure 6, which at least provide when and which SIE bands are most likely to be sensitive to global teleconnections. The SIE^* regions showing the strongest and most persistent extrapolar links in the observations are the western Indian, eastern Pacific sectors of the Antarctic and central Weddell Sea when SIE^* lags SAT^* from 0 months to 2 years. Conversely, the GISS results show a high fraction of grid points exceeding the 95% confidence level for zero lag and nearly all SIE^* regions

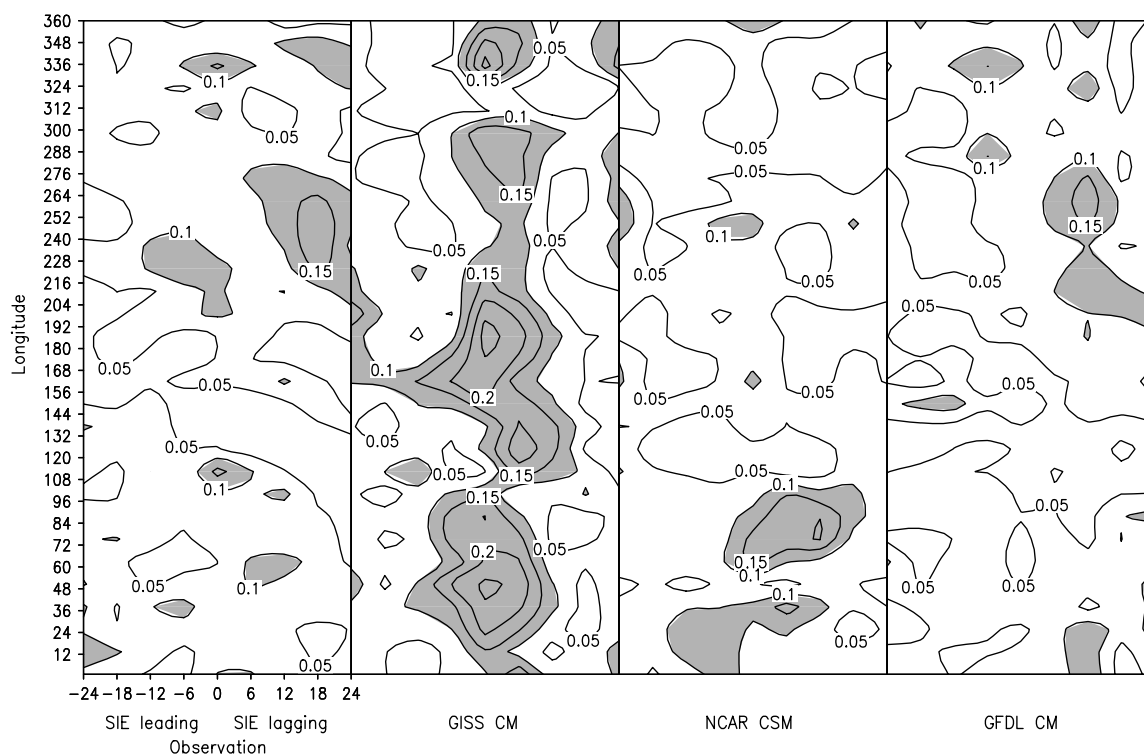


Figure 6. The fraction of total grid points in each correlation map that pass the local 95% significance test in the observation, GISS, NCAR and GFDL models with SIE^* leading 2 years to lagging 2 years (the fractions above 5% are shaded)

around the Antarctic. This reflects a strong circumpolar and broad Antarctic-wide coherency in that model (Figure 4(b1)). The SIE* regions linked to extrapolar climate in the NCAR model are the Indian with SIE* leading 6 months to lagging 1 year with respect to the SAT*. The GFDL model appears to capture those SIE* regions for which the observations show the strongest extrapolar links, but only when SIE* lags SAT* by a year.

In an attempt to differentiate signal from noise in the correlation maps (showing the global distribution of correlation coefficients), we performed an EOF analysis on 270 correlation maps for each model to detect the dominant and persistent teleconnection patterns between Antarctic SIE* and global SAT*. We then compared the EOF patterns with those arising from the correlations involving the observations. The first three modes of the observed correlation maps clearly display the main spatial patterns captured in the observed SAT* modes in Yuan and Martinson (2000), the Antarctic dipole and the meridional banding structure in the Pacific and Atlantic (Figure 7(a)). All the models show the ENSO-like pattern to some degree (Figure 7(b3),(c3) and (d2)), whereas the GFDL model appears qualitatively to look most like the observed patterns. The Antarctic dipole is represented in the third mode in each model. The GISS and NCAR models reproduce the meridional banding structure in the Pacific to a limited extent. Generally speaking, the models capture a reasonable fraction of the observed teleconnection patterns. However, all the models: (1) produce a weaker linkage between Antarctic SIE* and ENSO variability; (2) miss the strong teleconnection pattern observed in the western extreme of the tropical and southern Pacific, as well as over the tropical continents (South America and Africa).

5. DISCUSSION AND CONCLUSIONS

This study seeks to determine the extent to which three standard and well tested global climate models capture observed polar–extrapolar teleconnections documented in Yuan and Martinson (2000).

The Antarctic SIE characteristics and its global teleconnections, as exhibited by these models, are consistent with the observations to some extent. All models do a reasonable job simulating the seasonal advance and retreat of the Antarctic sea ice fields. Specifically, the GISS and NCAR models produce SIE distributions most similar to the observed SIE in summer and autumn, and the GFDL model does best in spring and winter. The observed dominant spatial covarying patterns in SAT variability, such as the ENSO-like pattern, are captured by all models to some extent. The negative correlation between (a) the western extreme of the tropical and southern Pacific and (b) eastern tropical Pacific and eastern Pacific sector of the Antarctic is partially captured by the NCAR and GFDL models. The simulated polar–extrapolar linkages between Antarctic SIE* and global SAT* in these models display a weak ENSO-like signal, similar to the observed teleconnection patterns. The GISS and NCAR models represent the Antarctic dipole and the meridional banding structure in the Pacific. Among the three models, the GISS model results seem to be moderately encouraging for studies on polar–extrapolar teleconnections, which might be attributed to its more complex sea ice dynamics (relative to the GFDL model) and the absence of sea ice extent constraints (relative to the NCAR model). Note that the model results analysed are from previously published standard model results, and do not include some of the newer, higher-resolution model results that may do a better job in simulating the polar–extrapolar covariability.

Despite some encouraging agreements between simulated SIE* and its global teleconnections relative to that documented in the observations, the models still differ from observations in some noteworthy ways. The observed SIE trends with their strong regional variability are not well simulated by the models. Excess sea ice cover is produced in the eastern Pacific sector of the Antarctic and the Weddell Sea in the GISS model in spring and winter due to the simulated colder and fresher sea water in the upper ocean layer, which encourages enhanced sea ice growth. This fresher water might be related to excess glacial ice calved into the ocean (compared with reported values in IPCC). Less simulated sea ice cover occurs between the eastern Indian and the western extreme of the western Pacific sectors of the Antarctic. On the contrary, the NCAR model produces less sea ice cover in the eastern Ross Sea, the eastern Pacific sector

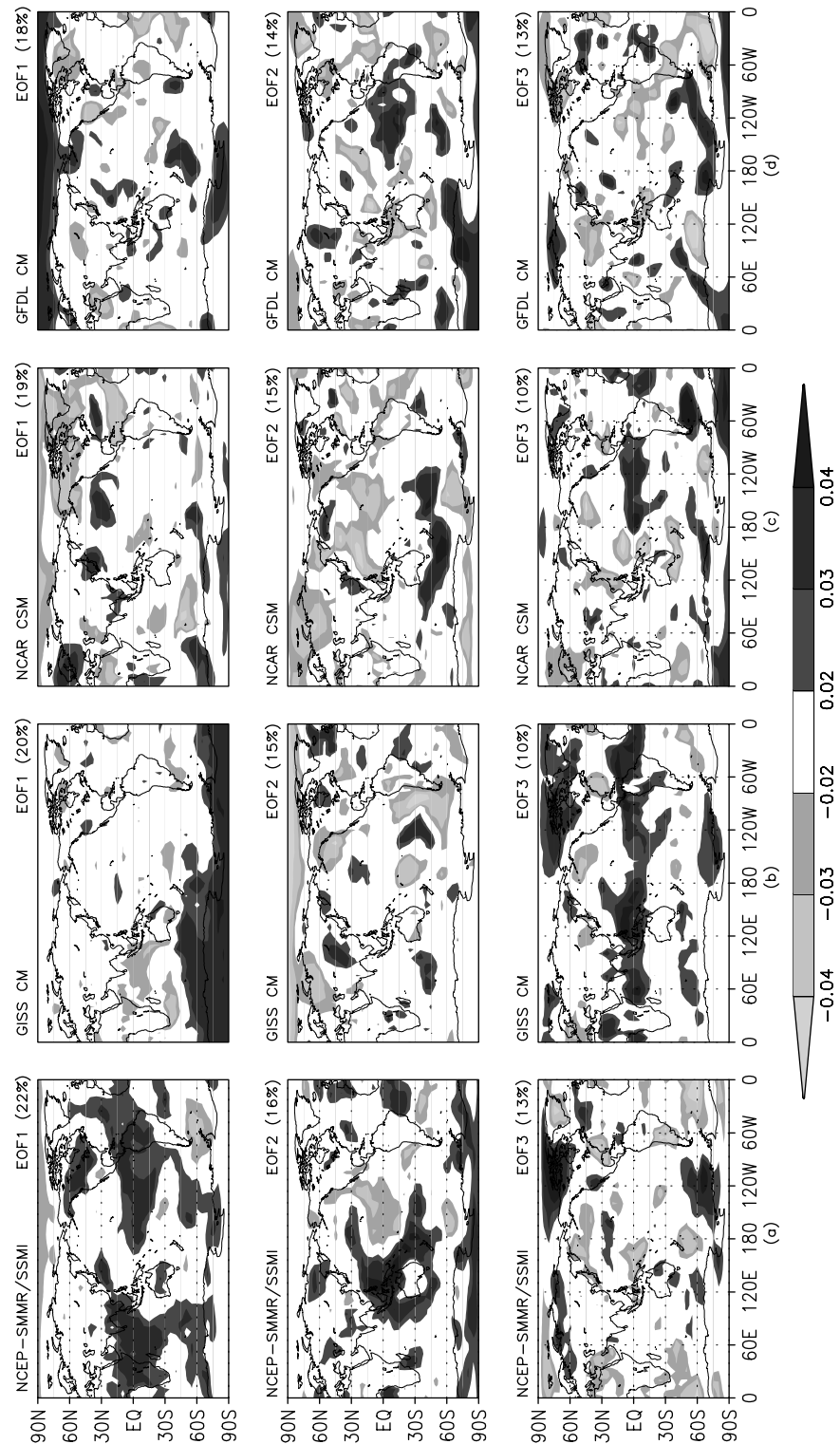


Figure 7. The first three leading EOF mode eigenvectors of correlation fields generated by correlating 30 Antarctic SIE* bands and global SAT* of the observations (a), GISS (b), NCAR (c) and GFDL (d) models at half-year intervals up to ± 2 years

of the Antarctic and the Weddell Sea in spring. The GFDL model generates more sea ice cover between the eastern Indian and western Pacific sectors of the Antarctic and in the Weddell Sea in summer and autumn. Although the models capture some of the observed spatial SAT* patterns and observed correlation patterns between Antarctic SIE* and global SAT*, the simulated linkage between Antarctic SIE* and ENSO variability is weak; some dominant observed teleconnection patterns (the Indian component of the ENSO-like pattern, a maximum magnitude in the western extreme of the tropical and southern Pacific, and the strong in-phase relationship between the tropical South America and Africa or TAV) are not well represented or are completely missed in the lag correlation maps and EOF analysis on those correlation maps of each model.

One can ask why, despite the inadequate SIE* characteristics and SAT* EOF performances themselves, some components of the cross-latitude teleconnections are still maintained. The reason for this is that the teleconnections are mainly the result of specific atmospheric dynamical reactions to meridional temperature gradient changes (Rind *et al.*, 2001). Whatever is causing the latitudinal temperature gradient changes in the models, then, produces some aspects of the realistic responses. In addition, each model has its own SIE regions sensitive to global teleconnections. Our results suggest that though global climate models have the capability to reflect some features of the SAT* variability and polar–extrapolar connectivities, they are not good at describing the detailed linkages between Antarctic SIE* and global SAT*. One underlying problem is probably that the models lack a dominant ENSO mode, which would clarify and force the proper responses. With more complicated sea ice dynamics, the GISS and NCAR models reproduce better observed polar–extrapolar teleconnections than the GFDL model, especially at zero lag (Figure 5). Therefore, more realistic sea ice dynamics and thermodynamics parameterizations might be desired to improve sea ice representation and complex air–sea-ice interactions, leading to proper polar–global covariability. We intend to perform some additional model experiments and analyses with the GISS model results, and if possible, with the other models, in an attempt to identify further the mechanisms responsible for generating the more realistic teleconnections in the models. Such an analysis has already been partially completed for the GISS model and presented in Rind *et al.* (2001). They found that ENSO variability drives changes in the Hadley cell, and moving the subtropical jet in the Pacific, with an opposite shift in the Atlantic due to influence of the Walker cell through equatorial subsidence in the Atlantic. This hemispheric mechanism also explains why the Antarctic dipole is out of phase.

ACKNOWLEDGEMENTS

This research was supported by NASA grants NAG 5-7922, NAGS-8725, the NASA polar programs and a NOAA award (UCSIO PO 10156283). The sea ice concentration data were provided by NOAA's National Snow and Ice Data Center. Lamont–Doherty Earth Observatory Contribution 6275.

REFERENCES

- Broccoli AJ, Manabe S. 1987. The influence of continental ice, atmospheric CO₂, and land albedo on the climate of the last glacial maximum. *Climate Dynamics* **1**: 87–99.
- Bryan K. 1969. Climate and the ocean circulation. III: the ocean model. *Monthly Weather Review* **97**: 806–827.
- Bryan K, Lewis LJ. 1979. A water mass model of the world ocean. *Journal of Geophysical Research* **84**: 2503–2517.
- Bryan FO, Kauffman BG, Large WG, Gent PR. 1996. The NCAR CSM flux coupler. NCAR Tech. Note NCAR/TN-425+STR; 48pp.
- Cavalieri DJ, Gloersen P, Parkinson CL, Comiso JC, Zwally HJ. 1997. Observed hemispheric asymmetry in global sea ice changes. *Science* **278**: 1104–1106.
- Flato GM, Boer GJ. 2001. Warming asymmetry in climate change simulations. *Geophysical Research Letters* **28**: 195–198.
- Flato GM, Hibler WD. 1992. Modeling pack ice as a cavitating fluid. *Journal of Physical Oceanography* **96**: 4589–4603.
- Gates WL, Henderson-Sellers A, Boer GJ, Folland CK, Kitoh A, McAvaney BJ, Semazzi F, Smith N, Weaver AJ, Zeng Q-C. 1996. Climate models—evaluation. In *Climate Change 1995: The Science of Climate Change*, Houghton JT, Meira Filho LG, Callander BA, Harris N, Kattenberg A, Maskell K (eds). Cambridge University Press: Cambridge, UK; 229–284.
- Gent PR, McWilliams JC. 1990. Isopycnal mixing in ocean circulation models. *Journal of Geophysical Research* **20**: 150–155.
- Gent PR, Bryan FO, Danabasoglu G, Doney SC, Holland WR, Large WG, McWilliams JC. 1998. The NCAR climate system model global ocean component. *Journal of Climate* **11**: 1287–1306.
- Gloersen P. 1995. Modulation of hemispheric sea-ice cover by ENSO events. *Nature* **373**: 503–504.
- Gloersen P, Campbell WJ. 1991. Recent variations in Arctic and Antarctic sea-ice covers. *Nature* **352**: 33–36.
- Gordon CT, Stern WF. 1982. A description of the GFDL global spectral model. *Monthly Weather Review* **110**: 625–644.

- Hansen J, Russell G, Rind D, Stone P, Lacis A, Lebedeff S, Ruedy R, Travis L. 1983. Efficient three-dimensional global models for climatic studies: models I and II. *Monthly Weather Review* **111**: 609–662.
- Hibler WD. 1984. Role of sea ice dynamics in modeling CO₂ increase. In *Climate and Climate Sensitivity*, vol. 29, Hansen JE, Takahashi T (eds). AGU: 238–253.
- Kalnay EC, Kamamustu M, Kistler R, Collins W, Deaven D, Gandin L, Iredell M, Saha S, Woollen J, Zhu Y, Chelliah M, Ebisuzalei W, Higgins W, Janowiak J, Mo KC, Ropelewski C, Wang J, Leetma A, Reynolds R, Jenne R, Joseph D. 1996. The NCEP/NCAR reanalysis project. *Bulletin of the American Meteorological Society* **77**: 437–471.
- Kattenberg A, Giorgi F, Grassl H, Meehl GA, Mitchell JFB, Stouffer RJ, Tokioka T, Weaver AJ, Wigley TML. 1996. Climate models — projections of future climate. In *Climate Change 1995: The Science of Climate Change*, Houghton JT, Meira Filho LG, Callander BA, Harris N, Kattenberg A, Maskell K (eds). Cambridge University Press: Cambridge, UK.
- Kiehl JT, Hack JJ, Bonan G, Boville BA, Williamson D, Rasch P. 1998. The National Center for Atmospheric Research Community Climate Model: CCM3. *Journal of Climate* **11**: 1131–1149.
- Kushnir Y, Rajagopalan B, Tourre Y. 1997. Decadal and multidecadal variability in Atlantic SST and SLP. *Atlantic Climate Variability Meeting Abstracts*.
- Large WG, McWilliams JC, Doney SC. 1994. Oceanic vertical mixing: a review and a model with a nonlocal boundary layer parameterization. *Reviews of Geophysics* **32**: 363–403.
- Lemke P, Harder M, Hilmer M. 2000. The response of Arctic sea ice to global change. *Climate Change* **46**: 277–287.
- Levitus S, Boyer TP. 1994. *World Ocean Atlas 1994 Volume 4: Temperature*. NOAA Atlas NESDIS 4. US Department of Commerce: Washington, DC; 117 pp.
- Levitus S, Burgett R, Boyer TP. 1994. *World Ocean Atlas 1994 Volume 3: Salinity*. NOAA Atlas NESDIS 3. US Department of Commerce: Washington, DC; 99 pp.
- Martinson DG. 1990. Evolution of the Southern Ocean winter mixing layer and sea ice: open ocean deepwater formation and ventilation. *Journal of Geophysical Research* **95**: 11 641–11 654.
- Meehl GA, Arblaster JM. 1998. The Asian–Australian and El-Niño–southern oscillation in the NCAR climate system model. *Journal of Climate* **11**: 1356–1385.
- Mitchell JF, Davis RA, Ingram WJ, Senior CA. 1995. On surface temperatures, greenhouse gases and aerosols: models and observations. *Journal of Climate* **8**: 2364–2386.
- NCAR OS (NCAR Oceanography Section). 1996. The NCAR CSM ocean model. NCAR Technical Note NCAR/TN-423+STR, NCAR, Boulder, Colorado.
- Pollard D, Thompson SL. 1994. Sea-ice dynamics and CO₂ sensitivity in a global climate model. *Atmosphere–Ocean* **32**: 449–467.
- Rind D, Healy R, Parkinson C, Martinson D. 1995. The role of sea ice in 2 × CO₂ climate model sensitivity. Part I: the total influence of sea ice thickness and extent. *Journal of Climate* **8**: 449–463.
- Rind D, Healy R, Parkinson C, Martinson D. 1997. The role of sea ice in 2 × CO₂ climate model sensitivity. Part II: hemispheric dependencies. *Geophysical Research Letters* **12**: 1491–1494.
- Rind D, Chandler M, Lerner J, Martinson D, Yuan X. 2001. The climate response to basin-specific changes in latitudinal temperature gradients and the implications for sea ice variability. *Journal of Geophysical Research* **106**: 20 161–20 173.
- Russell GL, Lerner JA. 1981. A new finite differencing scheme for the tracer transport equation. *Journal of Applied Meteorology* **20**: 1483–1498.
- Russell GL, Miller JR, Rind D. 1995. A coupled atmosphere–ocean model for transient climate change studies. *Atmosphere–Ocean* **33**: 683–730.
- Russell GL, Miller JR, Rind D, Ruedy RA, Schmidt GA, Sheth S. 2000. Comparison of model and observed regional temperature changes during the past 40 years. *Journal of Geophysical Research* **105**: 14 891–14 898.
- Semtner AJ. 1976. A model for the thermodynamic growth of sea ice in numerical investigations of climate. *Journal of Physical Oceanography* **6**: 379–389.
- Simmonds I, Jacka TH. 1995. Relationships between the interannual variability of Antarctic sea ice and the southern oscillation. *Journal of Climate* **8**: 637–647.
- Smith SR, Stearns CR. 1993. Antarctic climate anomalies surrounding the minimum in the southern oscillation index. In *Antarctic Meteorology and Climatology*, Bromwich DH, Stearns CR (eds). *Antarctic Research Series*, vol. 61 AGU: 149–174.
- Walsh JE. 1983. The role of sea ice in climate variability: theories and evidence. *Atmosphere–Ocean* **21**: 229–242.
- Weatherhead EC, Reinsel GC, Tiao GC, Meng XL, Choi D, Cheang WK, Keller T, DeLuise J, Wuebbles DJ, Kerr JB, Miller AJ, Oltmans SJ, Frederick JE. 1998. Factors affecting the detection of trends: statistical considerations and applications to environmental data. *Journal of Geophysical Research* **103**: 17 149–17 161.
- White BW, Peterson RG. 1996. An Antarctic circumpolar wave in surface pressure, wind, temperature and sea ice extent. *Nature* **380**: 699–702.
- Yuan X, Martinson DG. 2000. Antarctic sea ice variability and its global connectivity. *Journal of Climate* **13**: 1697–1717.